

Multiple relativistic outbursts of GRS 1915+105: radio emission and internal shocks

J.C.A. Miller-Jones,^{1*} D.G. McCormick,² R.P. Fender,³ R.E. Spencer,²

T.W.B. Muxlow,² and G.G. Pooley.⁴

¹*Astronomical Institute 'Anton Pannekoek', University of Amsterdam, Kruislaan 403, 1098 SJ, Amsterdam, The Netherlands.*

²*The University of Manchester, Jodrell Bank Observatory, Cheshire, SK11 9DL, UK*

³*School of Physics and Astronomy, University of Southampton, Highfield, Southampton, SO17 1BJ, UK*

⁴*Mullard Radio Astronomy Observatory, Cavendish Laboratory, Madingley Road, Cambridge, CB3 0HE, UK*

This is a preprint of an Article accepted for publication in MNRAS. © 2005 RAS

ABSTRACT

We present 5-GHz MERLIN radio images of the microquasar GRS 1915+105 during two separate outbursts in 2001 March and 2001 July, following the evolution of the jet components as they move outwards from the core of the system. Proper motions constrain the intrinsic jet speed to be $> 0.57c$, but the uncertainty in the source distance prevents an accurate determination of the jet speed. No deceleration is observed in the jet components out to an angular separation of ~ 300 mas. Linear polarisation is observed in the approaching jet component, with a gradual rotation in position angle and a decreasing fractional polarisation with time. Our data lend support to the internal shock model whereby the jet velocity increases leading to internal shocks in the pre-existing outflow before the jet switches off. The compact nuclear jet is seen to re-establish itself within two days, and is visible as core emission at all epochs. The energetics of the source are calculated for the possible range of distances; a minimum power of 1–10 per cent L_{Edd} is required to launch the jet.

Key words: Accretion, accretion discs – Stars:individual GRS1915+105 – Stars:variables – ISM: jets and outflows – Radio continuum:stars – X-rays:stars

1 INTRODUCTION.

GRS 1915+105 was the first Galactic source observed to exhibit superluminal motion (Mirabel & Rodríguez, 1994), and studies of its radio jets and jet-disc interactions have been important in developing our understanding of the link between accretion and jet outflows in X-ray binary systems. The jets extract mass, energy, and angular momentum from the accreting compact object, and in doing so can inject significant energy (≥ 1 per cent of the time-averaged luminosity of supernovae) into the ISM (Fender, Maccarone & van Kesteren 2005).

Jet outflows now seem to be ubiquitous in accreting systems such as black hole X-ray binaries. Such sources

spend the majority of their time in quiescence, with extremely low X-ray and radio luminosities and a relatively hard X-ray spectrum. In such states, they are thought to be ‘jet-dominated’, such that the power output in the jets exceeds that radiated in X-rays (Fender, Gallo & Jonker 2003). As the X-ray luminosity rises above $\sim 7 \times 10^{-5} L_{\text{Edd}}$, the systems become X-ray dominated, with the majority of the accretion energy being dissipated as X-rays in the inner parts of the accretion flow. The jets are then persistent, steady, and self-absorbed with a flat radio spectrum (Stirling et al. 2001; Dhawan, Mirabel & Rodríguez 2000b). At a high fraction ($\sim 10^{-1}$) of the Eddington luminosity, the central source makes a transition to a softer X-ray state, passing through the so-called Very High/Intermediate states. As this happens, the jet velocity increases, leading to internal shocks in the steady jet which appear as highly relativistic knots moving away from the core of the system (e.g. Fender et al., 1999). At this stage, the steady-state jet outflow is quenched

* email: jmiller@science.uva.nl

until the system moves back into its low/hard X-ray state once more. This unified model is presented for generic black hole X-ray binaries by Fender, Belloni & Gallo (2004), and for the specific case of GRS 1915+105 by Fender & Belloni (2004). We describe it in detail, and in the light of the observations we present, in § 8.

The source GRS 1915+105 was discovered in 1992 via the WATCH instrument aboard the Russian GRANAT mission (Castro-Tirado, Brandt & Lund 1992). The system is believed to comprise a K-M III star (Greiner et al., 2001a) and a $14 \pm 4 M_{\odot}$ black hole in a 33.5 ± 1.5 d orbit (Greiner, Cuby & McCaughrean 2001). The nature of the donor star implies that its mass should lie between 1 and $1.5 M_{\odot}$ and rules out the stellar wind as the accretion mechanism; the mass loss rate from such a star would be insufficient to feed the high accretion luminosity of GRS 1915+105. Thus it is thought that accretion occurs via Roche lobe overflow.

In this paper, we present a study of the 2001 March and July outburst of GRS 1915+105, using data from the Rossi X-ray Timing Explorer (*RXTE*) and the Multi-Element Radio Linked Interferometer Network (MERLIN). The X-ray observations are discussed in § 2 and the radio observations in § 3, which are used to place constraints on the jet speed and inclination angle, the source distance, and the possible deceleration and expansion of the jet knots as they move outwards from the core. The radio core emission is analysed in § 4, and polarisation maps are presented in § 5. We use the observations to constrain the energetics of the source in § 6, and address the discrepancy between radio observations of the jets in this source on different angular scales in § 7.

2 X-RAY STATES

The continuum X-ray spectrum of GRS 1915+105, in common with most other black hole sources, has been modelled as a superposition of a soft disc blackbody and a hard power law (e.g. Klein-Wolt et al., 2002). The blackbody ($k_{\text{B}}T \sim 1\text{--}2$ keV) is associated with the accretion disc, while the power law represents Comptonised emission from a corona, which latter component may be ejected leading to a radio flare (or oscillations in the case of repeated ejections). The X-ray emission is highly variable, which has been interpreted as the disappearance and reappearance of the inner region of the accretion disc (Belloni et al., 1997a,b), caused by the onset of thermal-viscous instabilities.

2.1 *RXTE* Data

RXTE, launched in 1995, carries two pointed instruments, the Proportional Counter Array (PCA) which covers the 2–60 keV energy range, and the High Energy X-ray Timing Experiment (HEXTE) for the 15–250 keV energy range. Using archival PCA data Belloni et al. (2000) found that the

X-ray variability is the result of transitions between three basic states; A, B, and C, categorised according to their spectral hardness, temporal variability, and the prominence of the thermal disc and power-law components.

The X-ray data presented here were collected by the All-Sky Monitor (ASM) on board *RXTE*, which scans about 80 per cent of the sky every orbit. The ASM returns the total source intensity in the 2–12 keV band as well as intensities in three sub-bands: A (1.3–3.0 keV), B (3.0–5.0 keV) and C (5.0–12.2 keV). Two hardness ratios can therefore be calculated; $\text{HR}_1 = B/A$ and $\text{HR}_2 = C/B$. It should be noted that the bands and ratios for the PCA differ due to that instrument’s higher energy range (2–60 keV) and that $\text{PCA HR}_1 \sim \text{ASM HR}_2$. The ASM count rates in the three bands and the HR_2 hardness ratio are shown in Figs. 1 and 2 for the March and July observations respectively. In all cases, the radio outbursts seem to be associated with a rise in the X-ray count rate and a degree of spectral softening (a decrease in the hardness ratio HR_2).

PCA observations were made during the March observations at the epochs indicated in Fig. 1, and in all cases, the temporal variability and spectral hardness showed the source to be in State C. PCA observations were also made during the July outburst, but since they have already been analysed by Vadawale et al. (2003), we will not reanalyse them here. They will be discussed in § 3.2.

3 OBSERVATIONS

GRS 1915+105 was observed with the MERLIN interferometer during two flaring sequences, between 2001 March 24 and 2001 April 5, and also between 2001 July 17 and 2001 July 24. The observing frequency was 4.994 GHz with a bandwidth of 15 MHz. The observing times are listed in Table 1. The March–April epochs of observation have been labelled 1–9 sequentially, and the July observations labelled 10–16. These target-of-opportunity observations were triggered by the ongoing flux monitoring program at the Ryle Telescope (Pooley & Fender, 1997). At each epoch, in addition to the target source GRS 1915+105, observations were made of a flux and polarisation angle calibrator, 3C 286, a point source calibrator, OQ 208, B 2134+004, or B 0552+398, and a phase reference source, B 1919+086, 2.8° away from the target source. The point source calibrator used, and the time on source for each epoch are also listed in Table 1. During the observations, the five outstations (Cambridge, Defford, Knockin, Darnhall and Tabley) were used, together with the Mark 2 antenna at Jodrell Bank.

The MERLIN d-programs were used to perform initial data editing and amplitude calibration, and the data were then imported into the National Radio Astronomy Observatory’s (NRAO) Astronomical Image Processing System (AIPS) software package for further data reduction. The MERLIN pipeline was then used to image and self-calibrate

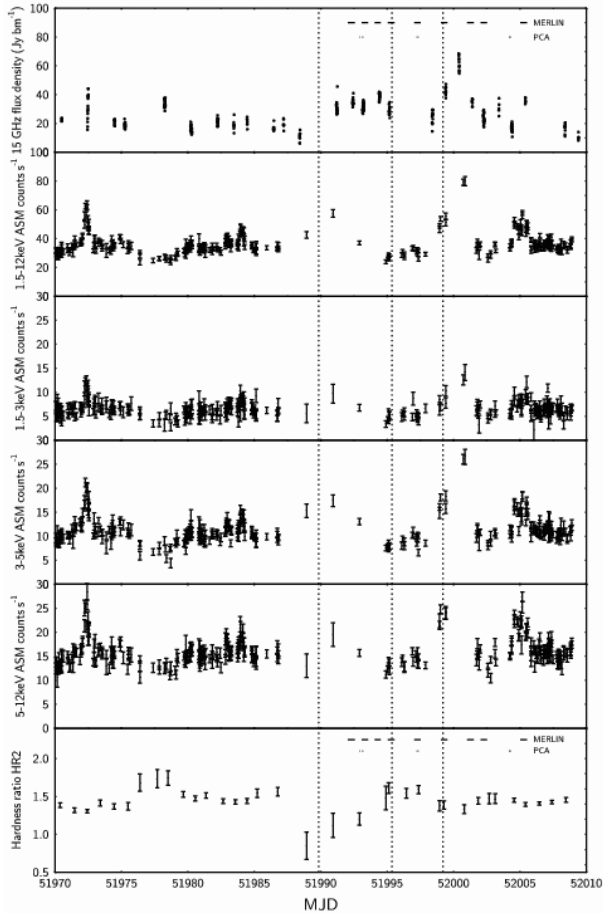


Figure 1. 15-GHz Ryle Telescope monitoring data, *RXTE* ASM count rates and hardness ratios prior to and during the 2001 March observations. Vertical dotted lines show the derived zero-separation times for the three ejected components, and the top set of horizontal lines in the radio and HR₂ plots show the times of our MERLIN observations. Below those are indicated the times of the *RXTE* PCA observations. Note the spectral softening and peak in the count rate at the time of the first ejection event.

the phase reference source, and apply the derived corrections to the target source, GRS 1915+105. The pipeline also calculated the instrumental corrections (the *D*-terms arising from signal leakage from right circular polarisation feeds into left, and vice versa) using B 1919+086, and calibrated the polarisation position angle using 3C 286, assuming a position angle of 33° east of north for its electric field vector. Further self-calibration and imaging were then carried out using standard procedures within AIPS, using the phase-referenced images as initial models for each epoch. The solution interval was gradually reduced and the number of CLEAN components used in the model was increased until there was no further improvement in the images. The images in Stokes *I*, *Q* and *U*, were then combined to produce images of total intensity, polarisation intensity, and polarisation position angle.

Epochs 1, 6, 7 and 12 were all found to show signifi-

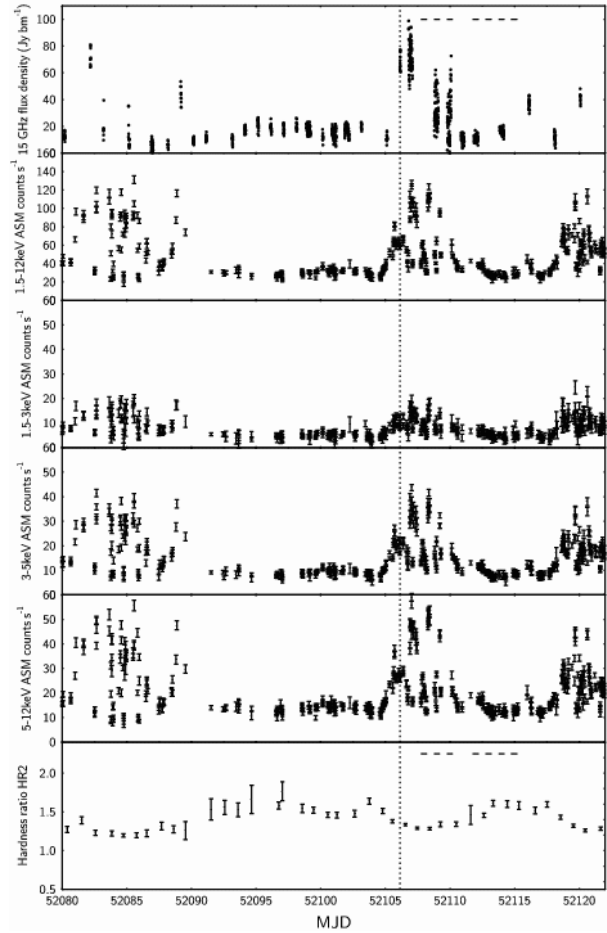


Figure 2. 15-GHz Ryle Telescope monitoring data, *RXTE* ASM count rates and hardness ratios prior to and during the 2001 July observations. Vertical dotted lines show the derived zero-separation times for the ejected component, and the horizontal lines in the radio and HR₂ plots show the times of our MERLIN observations.

cant core variability on timescales of tens of minutes over the course of the observing run. This made imaging difficult, as the sidelobe levels changed with time. For epochs 1 and 7, the core flux densities were approximately constant over a sufficiently long period of time that imaging and self-calibration using only a restricted time range was found to produce images with acceptably low residual r.m.s. noise levels. For epochs 6 and 12, the source flux densities were not constant for long enough for this approach to work. Instead, the data were split into small segments (of length 20 and 30 minutes respectively; a longer time period was required during the July observations since the source was intrinsically fainter). Each segment was self-calibrated to remove any atmospheric jitter, imaged, and the flux density of the core fitted and subtracted from the *uv*-data. The segments were then recombined, and the resulting core-subtracted data set was imaged to show any extension. A point source was added back in at the fitted core position, with the fitted mean flux density of the core, in order to make the final images seen

in Figs. 3, 5 and 12, and to enable easier comparisons to be made with the other epochs. The core parameters used were measured from the original image of the entire dataset for that epoch.

3.1 March outburst

Fig. 3 shows a composite of the MERLIN images of the March observations. The images have been rotated clockwise through 52.5° , so that the southeastern components appear on the left, and the northwestern components to the right. The core appears to be detected in all epochs (see § 4 for further discussion), and we clearly observe components moving away to the southeast and the northwest. The southeastern components appear to move faster (Fig. 4) and are brighter at a given angular separation from the core (Fig. 9), and thus correspond to the approaching jet, while the fainter, slower northwestern components are receding from us. This agrees with the findings of Mirabel & Rodríguez (1994), Rodríguez & Mirabel (1999) and Fender et al. (1999). Over the course of the 13 days of observation, three distinct southeastern components were seen to be ejected and move outwards, with the middle one being fainter than the first and last. These are labelled SE, SE2, SE3 respectively. Owing to Doppler deboosting of the receding jet flux density and its lower apparent proper motion, only a single northwestern component was observed, labelled NW. The fitted flux densities and angular separations from the core of the different components are given in Table 2.

Assuming that the ejecta move ballistically (i.e. with constant velocity), straight-line fits to the angular separations can be extrapolated to find the ejection dates of the different components. These are given in Table 4 and plotted in Fig. 4, and reveal that components SE and NW are consistent with having been ejected simultaneously. The quoted uncertainties take into account both the uncertainties in the fitted positions of the core and the jet component, and also the uncertainties in the time of observation, taken as half the length of the observing run. The Ryle telescope monitoring program (Pooley & Fender, 1997) indicates that the outburst in the 15-GHz flux density of GRS 1915+105 which triggered our MERLIN observations peaked at MJD 51990.4 (see Fig. 1). This, and also the observed sharp rise in 15-GHz flux density, is in good agreement with our zero-separation date of $\text{MJD } 51989.84 \pm 0.42$.

3.2 July outburst

Vadawale et al. (2003) carried out a detailed study of the X-ray and radio state of GRS 1915+105 prior to and during the July outburst. The outburst followed a by now familiar pattern, with a ~ 60 mJy 15-GHz radio flare on MJD 51989.0 (Vadawale et al., 2003) preceding a radio-loud plateau state, which lasted until the relativistic ejection. They found that according to the *RXTE* PCA observations, prior to July 16,

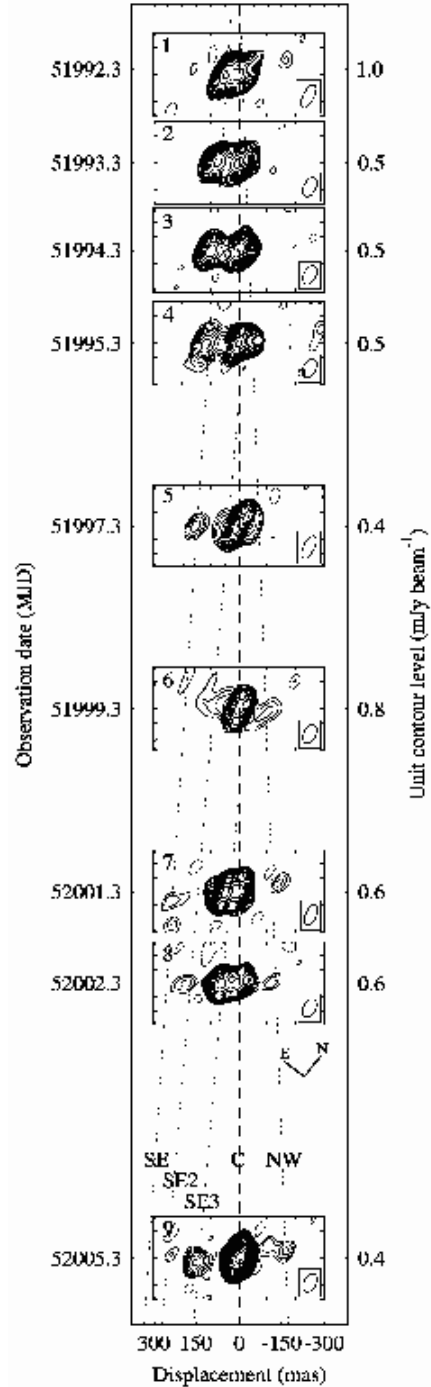


Figure 3. Contour maps for the March observations. Solid and dashed contours for each image are $(\sqrt{2}^n)$ and $-(\sqrt{2}^n)$ times the levels specified on the right-hand axis. The images have been rotated clockwise by 52.5° to form the montage. The dotted lines correspond to the fitted ejection dates and proper motions of the components. The vertical dashed line indicates the core position. The beam sizes for each image are plotted in the lower right-hand corner. At a distance of $d_{\text{max}} = 10.9$ kpc, 1mas on the image corresponds to a spatial scale of 10.9 au. The component labels are shown above the epoch 9 image, and the orientation on the sky is also indicated.

Table 1. The labels, dates, Modified Julian Dates and on-source times for the 2001 MERLIN observations of GRS 1915+105.

Epoch	Date (2001)	MJD	Time on source (min)	Point source calibrator
1	March 24	51992.30225 ± 0.25878	478.5	B 0552+398
2	March 25	51993.32289 ± 0.23779	438.9	B 0552+398
3	March 26	51994.27843 ± 0.23574	433.7	B 0552+398
4	March 27	51995.29641 ± 0.25411	468.0	B 0552+398
5	March 29	51997.28781 ± 0.24570	431.3	B 2134+004
6	March 31	51999.28593 ± 0.24383	447.9	B 0552+398
7	April 2	52001.27083 ± 0.25383	468.0	B 0552+398
8	April 3	52002.27575 ± 0.25403	468.4	B 0552+398
9	April 6	52005.25733 ± 0.22043	408.4	B 0552+398
10	July 17	52107.98903 ± 0.23861	372.1	B 0552+398
11	July 18	52108.98906 ± 0.23865	369.7	OQ 208
12	July 19	52109.98907 ± 0.23865	371.9	B 0552+398
13	July 21	52111.98906 ± 0.23865	375.8	OQ 208
14	July 22	52112.98282 ± 0.23239	357.7	OQ 208
15	July 23	52113.98278 ± 0.23236	361.1	OQ 208
16	July 24	52114.96038 ± 0.25060	388.3	OQ 208

Table 2. The fitted flux densities and angular separations from the core of components for the 2001 March observations of GRS 1915+105. The integrated flux densities and positions of the components were found by fitting Gaussians, and the angular separations were all measured from the fitted core positions in their respective images.

Epoch	MJD -51990	Core flux (mJy)	SE sep. (mas)	SE flux (mJy)	SE2 sep. (mas)	SE2 flux (mJy)	SE3 sep. (mas)	SE3 flux (mJy)	NW sep. (mas)	NW flux (mJy)
1	2.36 ± 0.20	38.2 ± 0.4	51.7 ± 2.2	31.4 ± 0.04						
2	3.32 ± 0.24	24.6 ± 0.3	75.8 ± 2.4	21.1 ± 0.03						
3	4.28 ± 0.24	29.4 ± 0.3	98.5 ± 2.5	19.0 ± 0.3						
4	5.30 ± 0.25	27.8 ± 0.5	112.6 ± 10.1	10.5 ± 0.6						
5	7.29 ± 0.25	19.4 ± 0.2	152.6 ± 15.6	1.6 ± 0.2	50.7 ± 18.3	2.3 ± 0.3			52.2 ± 17.0	2.8 ± 0.4
6	9.29 ± 0.24	49.7 ± 0.2							53.8 ± 29.5	1.9 ± 0.3
7	11.27 ± 0.10	26.9 ± 0.4	234.8 ± 32.1	2.1 ± 0.5			50.3 ± 1.9	51.1 ± 0.4	96.8 ± 60.3	4.9 ± 1.2
8	12.28 ± 0.25	19.6 ± 0.3			192.4 ± 28.0	2.2 ± 0.4	65.3 ± 2.4	26.4 ± 0.3	151.7 ± 21.1	1.6 ± 0.4
9	15.28 ± 0.25	94.3 ± 0.3			240.7 ± 67.7	0.6 ± 0.3	155.3 ± 7.7	4.2 ± 0.3	115.0 ± 28.9	1.5 ± 0.3
									167.7 ± 15.6	1.1 ± 0.2

the source was in a hard state (the radio-loud C-state, C_{RL}), in the χ_{RL} class, and then moved to a state of enhanced X-ray emission, possibly due to a disturbed accretion disc. They were however unable to determine the exact time of the X-ray state change. During the radio flare, they saw X-ray dips, corresponding to periods of state A, during which the Comptonised spectral component of the X-ray emission was absent.

During our July observations, from which the images are shown in Fig. 5, the flux densities of the core and the jet components were in general much lower than during the March observations. The flux densities of the core and SE component, and the angular separation between the two, are given in Table 3. The only epochs in which an unambiguous detection of the NW component was made were 12 and 13. There is marginal evidence in epoch 11 for an elongation of the core in the opposite direction to that of the SE jet component, which could be interpreted as the receding component. There may be a north-western extension to the core in epoch 14, though this is not particularly convincing (having a flux density of only 1–2 times the r.m.s. noise).

Again assuming ballistic motion, a straight-line fit to the angular separations of the SE component from the core gives a proper motion of $\mu_{app} = 23.8 \pm 2.7 \text{ mas d}^{-1}$. The fit is good, with $\chi_{red}^2 = 0.4$, and implies a zero-separation date of MJD 52106.1 ± 1.4 , which corresponds to July 16 03:21 UT, in good agreement with the start of the outburst determined by Vadawale et al. (2003). A similar fit to the receding component gives $\mu_{rec} = 11.8 \pm 3.5 \text{ mas d}^{-1}$, and a zero-separation date in agreement with that for the approaching component. These two fits are shown in Fig. 6.

3.3 Proper motions

For a symmetric ejection event, if the proper motions of corresponding approaching and receding components, μ_a and μ_r respectively, can be measured, it is possible to calculate the product

$$\beta \cos \theta = \frac{\mu_a - \mu_r}{\mu_a + \mu_r}, \quad (1)$$

Table 3. The fitted flux densities and angular separations of components from the core for the 2001 July observations of GRS 1915+105.

Epoch	MJD-52100	Angular separation (mas)	Error (mas)	Core flux density (mJy)	Error (mJy)	SE flux density (mJy)	Error (mJy)
10	7.99	42.1	4.1	28.0	0.6	33.6	0.8
11	8.99	71.1	6.6	27.1	0.4	8.9	0.4
12	9.99	90.9	27.9	27.7	0.5	2.6	0.5
13	11.99	150.2	30.6	9.6	0.4	2.0	0.4
14	12.98	158.1	70.8	15.1	0.3	0.6	0.3
15	13.98	179.0	48.7	15.1	0.3	1.2	0.4
16	14.96	204.3	29.7	16.3	0.3	0.8	0.3

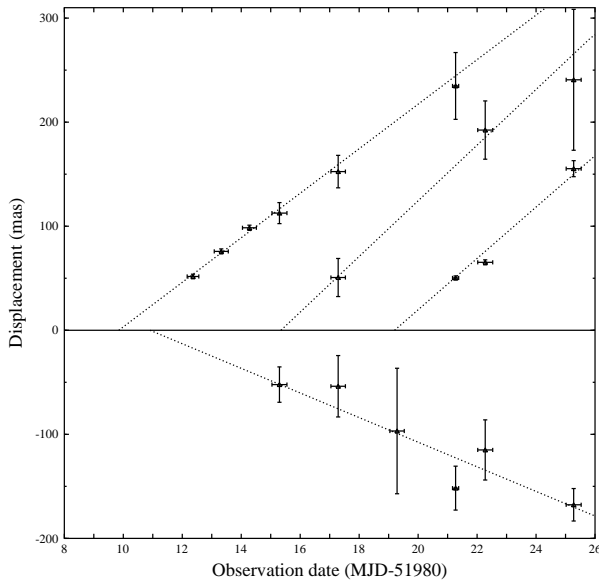
Table 4. Fitted proper motions and ejection dates of jet components, assuming ballistic motion

Outburst	Component	Epochs	Proper motion (mas d ⁻¹)	Ejection date (MJD)	χ^2_{red}
2001 March	SE	1-5,7	21.4 ± 2.0	51989.84 ± 0.42	1.08
2001 March	NW	4-9	11.8 ± 2.0	51990.9 ± 2.2	2.92
2001 March	SE2	5,8,9	26.8 ± 5.9	51995.4 ± 2.6	0.20
2001 March	SE3	7-9	27.4 ± 2.5	51999.6 ± 1.6	1.47
2001 March	SE3	6-9	24.7 ± 1.0	51999.2 ± 0.6	3.09
2001 July	SE	10-16	23.8 ± 2.8	52106.1 ± 1.4	0.41
2001 July	NW	0 ^a ,12-14	11.8 ± 3.5	52106.2 ± 3.8	0.11
1997 Oct	SE		23.6 ± 0.5 ^b		≤ 1
1997 Oct	NW		10.0 ± 0.5 ^b		≤ 1
1994 Mar	SE		17.6 ± 0.4 ^c		≤ 1
1994 Mar	NW		9.0 ± 0.1 ^c		≤ 1

^a To better constrain the fit, the zero-separation date ('epoch 0') derived from the fit to the SE component was also used

^b Data taken from Fender et al. (1999)

^c Data taken from Mirabel & Rodríguez (1994)

**Figure 4.** Proper motions for the March observations. The dotted lines correspond to the best fitting ejection dates and proper motions for the different components, accounting for uncertainties in both time of observation and measured angular separation.

where β is the jet speed v/c and θ is the inclination angle of the jet axis to the line of sight. Setting $\theta = 90^\circ$ allows us to place a lower limit, β_{min} on the intrinsic jet velocity. Assuming $\beta = 1$ places an upper limit, θ_{max} , on the inclination angle of the jet axis to the line of sight, and allows an upper limit, d_{max} , to be placed on the source distance, given by

$$d_{\text{max}} = \frac{c}{\sqrt{\mu_a \mu_r}}. \quad (2)$$

For μ_a and μ_r in units of mas d^{-1} , this may be more conveniently expressed as

$$d_{\text{max}} = \frac{173}{\sqrt{\mu_a \mu_r}} \text{ kpc}. \quad (3)$$

Assuming that the SE and NW components for the March outburst were the approaching and receding components from a single symmetric event, then from the fitted proper motions given in Table 4, we find $\beta \cos \theta = 0.29 \pm 0.09$. This gives $\beta_{\text{min}} = 0.29 \pm 0.09$, $\theta_{\text{max}} = 73.3 \pm 5.2^\circ$, and $d_{\text{max}} = 10.9 \pm 1.0$ kpc. If the distance is specified, then the exact values of β and θ can be calculated, as can the bulk Lorentz factor $\Gamma = (1 - \beta^2)^{-1/2}$, and the Doppler factors of the approaching and receding jets, $\delta_{\text{app,rec}} = (\Gamma[1 \mp \beta \cos \theta])^{-1}$. These have been plotted in Fig. 7.

We can also use the proper motions from the July

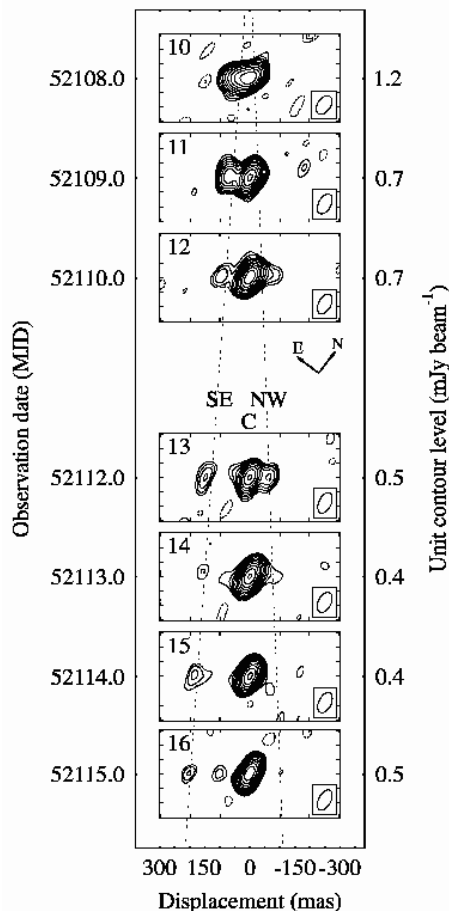


Figure 5. Contour maps for the July observations. Solid and dashed contours for each image are $(\sqrt{2}^n)$ and $-(\sqrt{2}^n)$ times the levels specified on the right-hand axis. The images have been rotated clockwise by 52.5° to form the montage. The dotted lines correspond to the fitted ejection dates and proper motions of the components. The vertical dashed line indicates the core position. The beam sizes for each image are plotted in the lower right-hand corner. At a distance of $d_{\max} = 10.9$ kpc, 1mas on the image corresponds to a spatial scale of 10.9 au.

outburst given in Table 4 to find $\beta \cos \theta = 0.34 \pm 0.14$, $\theta_{\max} = 70.4^\circ \pm 8.5^\circ$, and $d_{\max} = 10.3 \pm 1.6$ kpc. These are consistent with the values found for the March outburst, so for this reason, and since, owing to the more robust detection of the receding component, the March values were better-determined, the jet parameters for this outburst have not been plotted.

Our derived proper motions are consistent (to within errors) with those found by Fender et al. (1999) with MERLIN and Dhawan et al. (2000b) with the VLBA, but greater than those found by Mirabel & Rodríguez (1994) and Rodríguez & Mirabel (1999) with the VLA. The implications of this are discussed further in § 7.

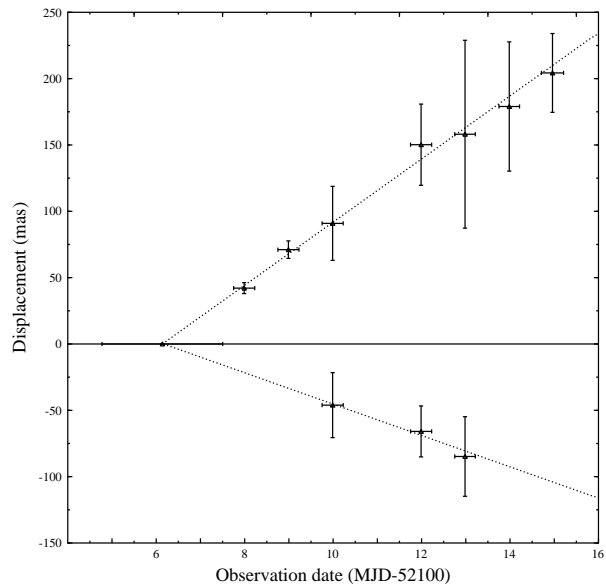


Figure 6. Proper motions for the July observations. The dotted lines correspond to the best fitting ejection dates and proper motions for the different components, accounting for the averaging time and the uncertainty in measured angular separation.

3.4 Source distance

Mirabel & Rodríguez (1994) originally derived a distance of 12.5 ± 1.5 kpc to GRS 1915+105 from H I absorption measurements with the VLA, while their measurements of jet knot proper motions constrained the maximum possible source distance (corresponding to $\beta = 1$) to be $d_{\max} = 13.7 \pm 0.2$ kpc. The proper motion observations of Fender et al. (1999) gave a somewhat smaller value, $d_{\max} = 11.2 \pm 0.8$ kpc. Dhawan, Goss & Rodríguez (2000a) further constrained the distance to GRS 1915+105, again using H I absorption measurements. They found $d \geq 6.1$ kpc and $d \leq 12.2$ kpc, and adopted a distance of 12 ± 1 kpc. They also found extra absorption along the line of sight to GRS 1915+105 compared with that to the H II region G 45.46+0.06 (at a distance of 8.8 kpc), implying $d > 9$ kpc. Recently however, Kaiser et al. (2004) interpreted the two *IRAS* sources identified by Rodríguez & Mirabel (1998) as the impact sites of the jets of GRS 1915+105 on the interstellar medium. This would require all three sources to be at approximately the same distance from us, $6 \leq d \leq 7.4$ kpc. They also pointed out that the CO observations of Chapuis & Corbel (2004) allowed the constraint on the distance being beyond the G 45.46+0.06 to be relaxed. Zdziarski et al. (2005) dismissed these assertions however, claiming that systematic errors on the systemic velocity derived from infrared CO lines by Greiner et al. (2001b) would be small. The systemic velocity of Greiner et al. together with the Galactic rotation curve gave a distance of 12.1 ± 0.8 kpc. Our 3σ upper limits on d_{\max} for the March and July outbursts are 13.9 and 15.1 kpc respectively.

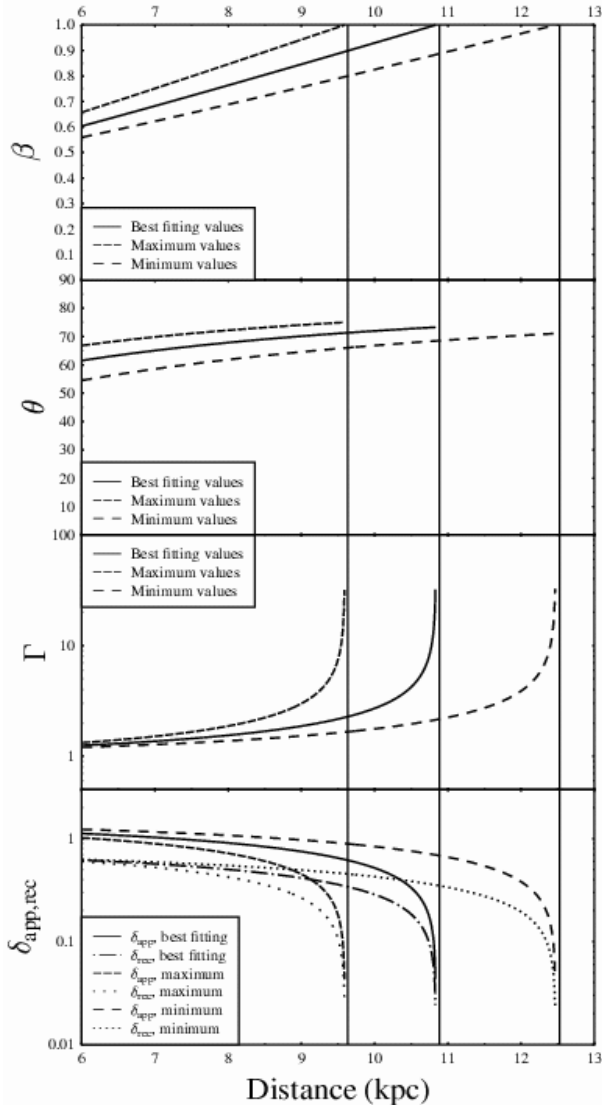


Figure 7. Variation with assumed source distance of jet speeds, inclination angles, bulk Lorentz factors and Doppler factors for the approaching and receding jets. Calculations have been done for the best fitting proper motions, the proper motions both low by 1σ (minimum values), and the proper motions both high by 1σ (maximum values). The vertical lines indicate the values of d_{\max} , 10.9, 12.5, and 9.5 kpc respectively.

In summary, the distance would appear to lie between 6.1 and 12.2 kpc, implying intrinsic jet speeds of $0.57 < \beta < 1$, from our observations and Fig. 7. But it is not yet possible to break the degeneracy between jet speed and inclination angle and place any more rigorous constraints on the intrinsic jet speeds. Dhawan et al. (2000b) suggested that measurement of the annual trigonometric parallax (~ 80 mas) might in future resolve this discrepancy. Such a measurement would seem to be of prime importance in deciding how relativistic the jets from this source actually are, and in constraining the energy budget of the outbursts.

Fender (2003) remarked that all significantly relativistic jets lie very close to d_{\max} (which is in fact implicit in the definition of d_{\max} since it is the source distance corresponding to $\beta = 1$). If the jets in GRS 1915+105 are as relativistic as has previously been claimed (Mirabel & Rodríguez, 1994; Fender et al., 1999), the source is certainly at a distance of more than 9 kpc. Should it be as close as 6–7 kpc, as postulated by Kaiser et al. (2004), the jets, while fast, would not be the superluminal ejecta often assumed.

3.4.1 Are the knots decelerating?

As the jet knots move outwards, their bulk kinetic energy will be thermalised as they interact with their environment. Depending on the rate at which this process occurs, it might be possible to measure the deceleration of the jet knots, as has been done on arcsecond scales for the case of XTE J 1550–564 (Corbel et al., 2002). The internal shock model of Kaiser, Sunyaev & Spruit (2000) however, predicts that for a strong shock (which is believed to be the case), the velocity of the shock would be constant. In the case of GRS 1915+105, Mirabel & Rodríguez (1994) measured significantly slower proper motions for both the approaching and receding components than found here, at angular separations of up to 720 mas from the core. However, their data were consistent with ballistic motion, so deceleration would not seem to explain the discrepancy.

Fitting our measured angular separations with a quadratic function, rather than the straight-line fit required by ballistic motion, showed no conclusive evidence for deceleration. The best-fitting values for the three components where there were a sufficient number of measurements to properly constrain the fits (March SE, NW and July SE) were decelerations of 0.7 ± 0.5 , 0.4 ± 0.8 , and 0.9 ± 1.3 mas d⁻² respectively, all consistent with zero. The χ^2_{red} values of these fits were similar to those for the straight-line fits, and an F -test (e.g. Pfenniger & Revaz, 2005) showed that in no case was the probability greater than 95 per cent, i.e. adding in the deceleration parameter was not necessary at any significant level. Furthermore, the quadratic fit to the angular separation of the March SE component predicts an ejection date of MJD 51990.40 ± 1.5 , the date of the 15-GHz flux density peak. Assuming that the core flare corresponds to the ejection of that component, the ejection date would then have been prior to the flux density peak, strengthening the case against deceleration of that component in our data. These data do not therefore support the case for deceleration.

3.5 Expansion of jet components

While no clear expansion of the jet component sizes is seen in the images themselves, it should be remembered that the images of Figs. 3 and 5 are convolved with the Gaussian restoring beam of $\sim 75 \times 40$ mas². Deconvolving the beam

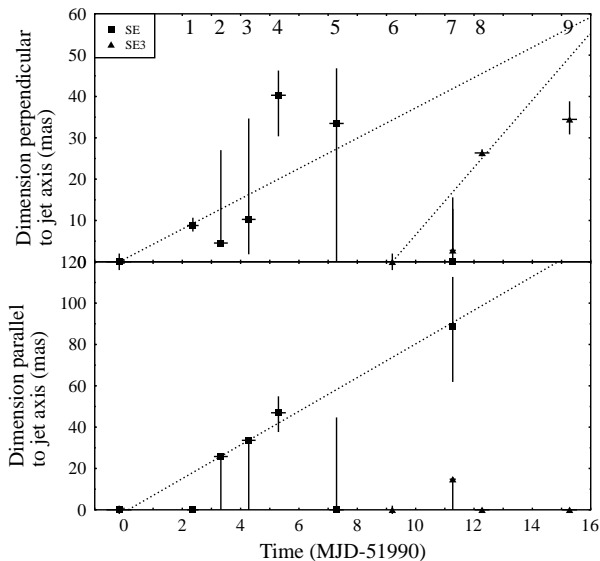


Figure 8. Deconvolved component sizes for components SE and SE3 of the March observations, perpendicular (top) and parallel (bottom) to the jet axis. Dotted lines show best-fitting linear expansions. Labels denoting the epochs of observation are shown in the top plot.

from the fitted sizes to find the intrinsic sizes of the Gaussian components fitted to the images shows marginal evidence for the expansion of the jet knots. Fig. 8 shows fitted Gaussian knot sizes parallel and perpendicular to the jet axis for components SE and SE3 of the March observations. Component SE only shows convincing evidence for being resolved perpendicular to the jet axis during epochs 1 and 5, whereas component SE3 shows significant evidence for being resolved in both epochs 8 and 9. The July observations were less conclusive, with the deconvolved component sizes initially seeming to increase, but falling off again in the later epochs as the flux density decreased and the knots became harder to detect.

If this component expansion is real, it can be used to constrain ϕ , the opening angle of the jet. We see the motion of the jet knots projected on the plane of the sky. This means that for a given angular separation, $\delta\psi$, the true separation of the knot from the core is $\delta\psi/\sin\theta$. Thus, assuming spherical jet knots,

$$\tan\phi = \frac{\dot{\zeta}\sin\theta}{\mu_{\text{app}}}, \quad (4)$$

where $\zeta = r/d$ is the angular size of the source. Without knowing the exact source distance, we have only an upper limit to the inclination angle of the jet axis to the line of sight. Taking only the most reliable point from the evolution of the SE component, that of epoch 4, gives $\dot{\zeta} = 7.4 \pm 1.5 \text{ mas d}^{-1}$, assuming zero size at the ejection date derived in § 3.1. Alternatively, a linear fit to the data (shown as the dotted line in Fig. 8) gives a value $\dot{\zeta} = 3.7 \pm 0.5 \text{ mas d}^{-1}$. These two values give upper limits on the jet cone half-opening angle of $\phi_{\text{max}} = 18.3^\circ \pm 3.5^\circ$ and $9.4^\circ \pm 1.3^\circ$ for the

SE component. Since the receding component corresponding to knot SE3 is not detected, θ_{max} is not well-constrained in that case.

At a distance of $d_{\text{max}} = 10.9 \text{ kpc}$, an angular expansion of $7.4 \pm 1.5 \text{ mas d}^{-1}$ corresponds to a lateral expansion speed of $0.47 \pm 0.10c$. We note that this is close to the theoretical expansion speed of a relativistic plasma, $c/\sqrt{3} = 0.58c$. The data are unfortunately not good enough to make a more detailed comparison possible in this case however.

3.6 Flux densities

Accurately measuring the flux densities of the components is a difficult procedure, since in order to adequately sample the uv -plane, and hence be able to detect the source structure, a long integration is required. But the jet components change in both position and flux density with time. During a 12-hour observation, the proper motion of 21.4 mas d^{-1} will cause a component to move by 10.7 mas.

For the early epochs where the jet component was sufficiently bright for its flux density to be determined accurately in a short time, the core was subtracted from the data in the uv -plane, and the flux density at the position of the extension was measured as a function of time using a direct Fourier transform of the complex visibilities, binning the data into 6-minute time intervals. At flux densities below $\sim 5 \text{ mJy beam}^{-1}$, the noise level in the data made this impossible, and the flux density of the extension had to be measured by fitting a Gaussian to the extension in the image plane. The receding component was at no time sufficiently bright to use the direct Fourier transform method.

Fitting a power-law decay with time to the measured flux densities for components SE and SE3, and constraining the ejection time to be the extrapolated time of zero-separation given in Table 4, gave power-law indices of 1.8 ± 0.03 and 2.01 ± 0.02 respectively, with χ_{red}^2 values of 3.9 and 1.7 respectively. The indices are Lorentz invariant, so are also applicable to the flux density decay in the knot frame (Rodríguez & Mirabel, 1999). Since the motion appears to be ballistic (§ 3.4.1), the flux density decays with angular separation with the same power-law index.

3.6.1 Flux density ratios

The ratio between the flux densities of approaching and receding components, S_{app} and S_{rec} respectively, measured at equal angular separation from the core, is given by

$$\frac{S_{\text{app}}}{S_{\text{rec}}} = \left(\frac{1 + \beta \cos\theta}{1 - \beta \cos\theta} \right)^{k+\alpha}, \quad (5)$$

where α is the spectral index of the emission, defined by $S_\nu \propto \nu^{-\alpha}$, where S_ν is the flux density at frequency ν . $k = 2$ for a continuous jet, and $k = 3$ for a jet composed of discrete

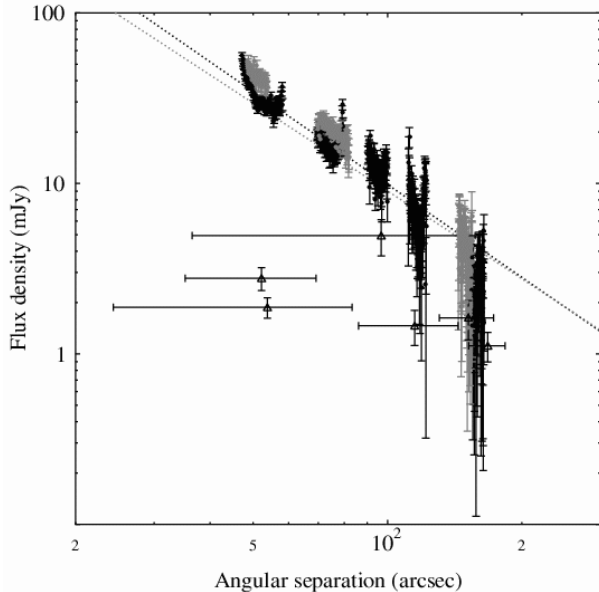


Figure 9. Decrease in flux density with angular separation from the core, for the March observations. Black points show the approaching component SE, grey points SE3, and open triangles the receding component NW. Dotted black and grey lines show the best-fitting power law decays for components SE and SE3. Flux densities for the approaching components were measured with time, converted to angular separations using the best-fitting proper motions for the two approaching components.

ejecta. However, as pointed out by Fender (2003), a measurement of the flux density ratio gives no information in addition to that already found from the proper motion analysis of § 3.3, other than the value of the k -parameter. Nevertheless, we can attempt to estimate this parameter from the data. The derived proper motions and zero-separation dates of the approaching components were used to convert the flux density decay with time found in § 3.6 to flux density as a function of angular separation from the core for the approaching component. Making a comparison to the flux density of the receding component should yield a flux density ratio *measured at equal angular separation*. However, Fig. 9 shows that this is not a straightforward procedure for these data. At small angular separations, where the flux density is high enough to be accurately measured, but the angular separations are less accurate, the flux density ratio is of order 10–15. At greater angular separations, the errors on the flux density determination are high, but the ratio is closer to 4–5. It appears that the flux density of the receding component is still rising up to an angular separation of ~ 100 mas, although the uncertainties on the data are large, so the flux density ratio is not constant as a function of angular separation. We now turn to a different approach to measuring k .

Miller-Jones, Blundell & Duffy (2004) derived an expression relating the value of $\beta \cos \theta$ to the flux density ratio in a single image, assuming adiabatic expansion of the jet components, with the knot radius scaling linearly with time.

In such a case, the flux density ratio *in a single image* is given by

$$\frac{S_{\text{app}}}{S_{\text{rec}}} = \left(\frac{1 + \beta \cos \theta}{1 - \beta \cos \theta} \right)^{k-p}, \quad (6)$$

where p is the index of the electron spectrum, such that $N(E) = \kappa E^{-p}$. We note however that if the rise phase was optically thin, and the image used was made at a time when the flux density of the receding jet was still increasing while that of the approaching jet was decreasing owing to adiabatic expansion, then this formalism would be invalid, since both knots must be in the adiabatic expansion regime of decreasing flux density. As already remarked, Fig. 9 appears to show that the flux density of the receding knot is still rising up to an angular separation of ~ 100 mas (with a large error bar), and only after that does it start decaying, so care must be taken when applying the above formalism.

The only epochs for which corresponding approaching and receding jets were both clearly visible and distinguishable from the core were 5, 7, and 13. These gave flux density ratios of 0.89 ± 0.17 , 1.27 ± 0.47 , and 0.76 ± 0.19 respectively. We note that in two of the three cases, the receding jet is brighter than the approaching jet, and the third case is in fact consistent with this scenario. This would constrain $k < p$. Since we do not have multiwavelength observations, it is not possible to deduce the spectral index of the jet knots, and hence the value of $p = 2\alpha + 1$. However, Fender et al. (2002) observed this same outburst at both 4.8 and 8.64 GHz, and found a spectral index for the integrated (core plus jet knots) flux density of the source which stabilised at $\sim 0.77 \pm 0.05$ by MJD 51991.9. Mirabel & Rodríguez (1994) measured a spectral index of 0.84 ± 0.03 for both the approaching and the receding jet components (once they had separated from the core) in the outburst of 1994 March. Assuming that the spectral index was the same in the outbursts we observed, this yields $k = 2.5 \pm 0.3$ for epoch 5, $k = 3.1 \pm 0.6$ for epoch 7, and $k = 2.3 \pm 0.4$ for epoch 13. These are significantly greater than the values of 1.3–1.9 found by Fender et al. (1999), but consistent with the value of 2.3 found by Mirabel & Rodríguez (1994), and would seem to imply something intermediate between discrete ejections and a steady jet. The high value for epoch 7 would seem to argue for a discrete ejection. However, it would seem strange for the character of the outburst (i.e. the value of k) to change as the knots moved outwards. A possible reason for the discrepancy could be that the formula was not applicable during epochs 5 and 13. The angular separation of the receding component during epoch 5 is 53.8 ± 29.5 mas which, from Fig. 9, would imply that k cannot be calculated accurately for this epoch using Equation 6, thus lending more credibility to the value derived for epoch 7. Since we have no similar plot for the July outburst, it is not possible to evaluate whether or not such an effect could also explain the low value of k for epoch 13.

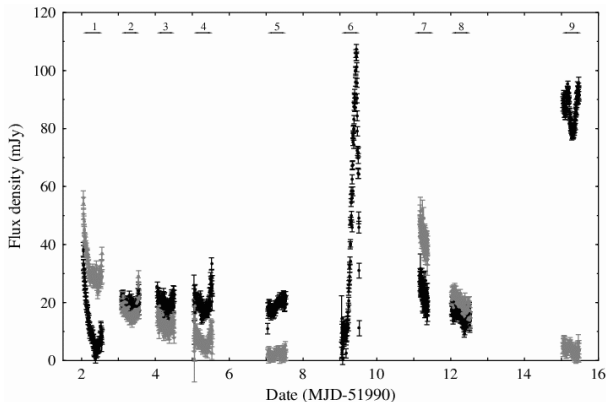


Figure 10. Flux density of the core during the 2001 March observations. The time range of each observation epoch is indicated at the top of the plot. Epochs 1, 6 and 7 all show a fractional variation of at least 50 per cent. The black points are for the core, and the grey points are for the approaching component, SE for epochs 1–5, and SE3 for epochs 7–9.

4 THE CORE

Detectable emission seems to be associated with what we interpret as the core of the system at all epochs, although in some of the observations it appears to be blended with an emerging approaching or receding jet component. This is in contrast to the observations of Fender et al. (1999) in which the flux density was always dominated by the jet components. Fig. 10 shows the flux density of the core and jet components during the March observations. As will be explained further in §5, the core was not in general found to show significant linear polarisation, except possibly for epochs 2 and 9 of the March outburst sequence.

Epochs 1 and 6 show that the core flux density faded to very low levels immediately after a flare. This can be identified as the jet suppression in the soft disc-dominated state in the model of Fender et al. (2004) (see § 8 for details). However, by the start of epoch 2, the core flux density had recovered and stabilised at a level of approximately 20 mJy. We attribute this low-level radio emission to the steady, compact nuclear jet. This stable level of ~ 20 mJy at 5 GHz was also seen following the July outburst. This implies that the source has moved back to a harder X-ray state to the right of the jet-line (see § 8 for further details) *without* launching a second major ejection. Only crossing the line from right to left in fig. 7 of Fender et al. (2004) (hard to soft X-ray state) gives rise to the internal shocks and the corresponding relativistic ejecta.

The flare in core flux density seen during epoch 6 of the March observations (Fig. 11) corresponds to the ejection of component SE3. The core flux density began to rise from a flat base level of 9.8 ± 1.2 mJy at MJD 51999.20 \pm 0.02, peaking at 107.4 ± 1.4 mJy 0.24 d later. Assuming the start of the rise phase to be the ejection date of the component, we

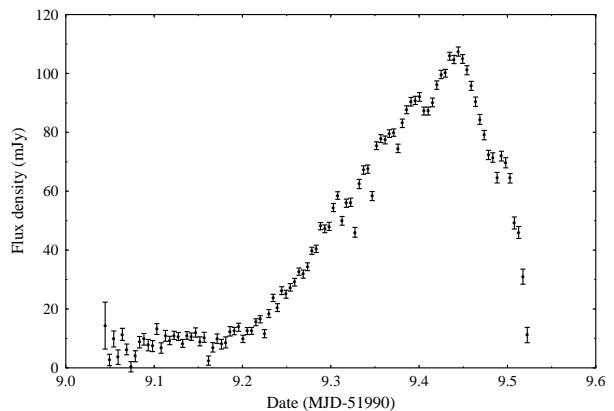


Figure 11. Flux density of the core during epoch 6 of the 2001 March observations. This does not follow the fast rise and exponential decay (FRED) behaviour observed for the integrated flux density of such systems. Note the rise from and fall back to very low flux densities (≤ 10 mJy) either side of the core flare.

get an extra constraint on the proper motion of component SE3, used in the fit for epochs 6–9 given in § 3.2 and Table 4.

A detailed inspection of Fig. 11 seems to show evidence for slightly more variable radio emission immediately prior to the rise in flux density corresponding to the flare, as originally noted by Fender et al. (2004). But we note that this, together with the rapid falloff in flux density at the very end of the observing run, occurred when the source elevation was low ($\lesssim 15^\circ$), at which point the weather begins to affect the gain solutions (otherwise good to ~ 5 per cent). A check on the flux density of the phase calibrator confirmed that only for the time range covering the last two points in Fig. 11 were the data thus affected. The rest of the data show that the core jet flux density decreased with an e-folding time of ~ 0.07 d. The data from epoch 1 show a very low core flux density (observed when the source was still at a fairly high elevation ($\sim 35^\circ$)). This is 2.5 ± 0.4 d after the derived ejection date of the SE component, by which time the jet knot would have moved out to an angular separation of ~ 55 mas, i.e. out of the beam. We cannot accurately probe the core flux density on its own until this time, as we will be unable to decouple the core emission from the jet knot emission. But the low flux density seen during epoch 1 suggests that the steady core jet is not re-established until the increase in core flux density 2.6 d after the ejection event. This is considerably longer than the timescale of 18 h found by Dhawan et al. (2000b) for the nuclear jet to reform following the start of a major outburst, derived from the date of the first observations (Fender et al., 1999) of radio oscillations following the outburst.

No short-period (20–40 min) oscillations of the core flux density such as those described by Pooley & Fender (1997) were observed. A search was made by measuring the flux density in the uv -plane at the core position in 1-minute time bins, having subtracted off any extension from the data. The resulting time series was run through one-dimensional

CLEAN algorithm (Roberts, Lehár & Dreher 1987), which showed no significant peaks in the power spectrum of the data on frequencies shorter than 2 d^{-1} .

The flux density of the core was much higher during epoch 9, at round 80-100 mJy, and seemed to oscillate with a period of approximately 8 hours. We cannot however determine whether these are true oscillations, since we only sample ~ 1.5 of these ‘periods’ in a 12-hour observing run.

4.1 Positional accuracy

The beam sizes for the various images are shown in Figs. 3 and 5. But the use of phase referencing allows the determination of the target position to much greater accuracy, set by the uncertainty in the position of the phase calibrator, the uncertainty in the telescope positions, and atmospheric phase winding. B 1919+086 has a position accurate to $\approx 14\text{ mas}$ (Browne et al., 1998), and being 2.84° from GRS 1915+105, introduces a positional uncertainty of about 10 mas if the atmosphere causes phase wraps on timescales of about 2 hours (the worst-case scenario in the data).

The positions of the core component were measured prior to self-calibration for each epoch, and a weighted mean position was taken for the July observations. This gave a B 1950 position of $19^{\text{h}}12^{\text{m}}49^{\text{s}}.96941 \pm 0^{\text{s}}.00009$, $10^\circ 51' 26''.6427 \pm 0.0051$, with a spread of 0.25 ms in RA and 15 mas in Dec. Owing to the multiple ejections during the March observations, the core position was harder to measure accurately, owing to the blending of the core with newly-emerging components. This led to a much greater spread in the measured core co-ordinate, of 2.67 ms in RA (1.12 ms neglecting epoch 7) and 17.1 mas in Dec. The weighted mean position was $19^{\text{h}}12^{\text{m}}49^{\text{s}}.96945 \pm 0^{\text{s}}.00053$, $10^\circ 51' 26''.6588 \pm 0.0060$ (B 1950). We note that these positions all rely on having correctly identified the relatively stationary central component in the images as the core. Furthermore, the systematic errors in the astrometry mentioned in the previous paragraph mean that the uncertainty on these derived absolute positions is at least of order 15 mas, although we did not have an astrometric check source we could use to quantify accurately this uncertainty. Since the hour angle coverage was approximately the same within the each set of observations (March and July), and since the same phase calibrator source was used in all observations, the errors in the relative positions from epoch to epoch are much smaller, and are dominated mainly by the signal-to-noise ratio and the atmospheric phase winding. The major source of error in the angular separations within a single image is the signal-to-noise ratio of the knots.

The most accurate determination of the position of the core of GRS 1915+105 is currently (Dhawan et al., 2000b) $19^{\text{h}}15^{\text{m}}11.^{\text{s}}54938 \pm 0.^{\text{s}}00007$, $10^\circ 56' 44.''7585 \pm 0.''001$ (J 2000) on 1998 May 2. The proper motion on the sky was determined as $5.8 \pm 1.5\text{ mas yr}^{-1}$, ascribed to secular parallax. In the three months separating our sets of observations,

Table 5. Polarisation parameters for the 2001 observations of GRS 1915+105. P is the polarised flux density, P/I is the fractional polarisation, and P.A. is the polarisation position angle. Where there was no detection, the 3σ upper limits have been given.

Epoch	Component	P (mJy)	P/I	P.A.
1	Core	0.67 ± 0.08	0.017 ± 0.002	$54.6 \pm 5.1^\circ$
1	SE	5.80 ± 0.09	0.184 ± 0.004	$-67.0 \pm 0.7^\circ$
2	SE	3.59 ± 0.10	0.170 ± 0.005	$-65.8 \pm 1.1^\circ$
3	SE	1.63 ± 0.09	0.086 ± 0.005	$-51.9 \pm 2.3^\circ$
4	SE	1.50 ± 0.13	0.143 ± 0.015	$-49.8 \pm 3.6^\circ$
4	NW	0.65 ± 0.12	0.236 ± 0.056	$-82.0 \pm 7.2^\circ$
5		< 0.32		
6		< 0.43		
7	SE3	5.14 ± 0.09	0.121 ± 0.003	$-61.9 \pm 0.8^\circ$
8	SE3	3.54 ± 0.10	0.134 ± 0.004	$-59.6 \pm 1.2^\circ$
9	Core	3.52 ± 0.16	0.037 ± 0.002	$73.1 \pm 5.1^\circ$
10	SE	2.79 ± 0.11	0.083 ± 0.007	$-90.2 \pm 3.8^\circ$
11	SE	0.63 ± 0.09	0.070 ± 0.010	$-77.8 \pm 5.8^\circ$
12	SE	0.31 ± 0.16	0.119 ± 0.066	$-74.7 \pm 15.1^\circ$
13		< 0.49		
15		< 0.49		
16		< 0.53		

this corresponds to a shift of $1.8 \pm 0.5\text{ mas}$ between our March and July observations. Our uncertainties are not sufficiently small to be able to verify this figure. However, comparison between our position and that of Dhawan et al. (2000b) is difficult, since the two sets of observations used different calibrators for the phase referencing, and since MERLIN uses B 1950 co-ordinates whereas the VLBA uses J 2000 co-ordinates.

5 POLARISATION

5.1 Linear polarisation

Polarisation images were made for all epochs, except epoch 14 (July 22), when the polarisation angle calibrator 3C 286 was not observed. Table 5 details the polarisation properties of the detected components. Since the overall flux density of the source was relatively lower during the July observations, polarisation was not detected at a significant level in the SE component after epoch 12, which itself only had a 2σ detection, and no significant core polarisation was detected at any time. The polarisation maps are shown in Fig. 12, and typically have a r.m.s. noise level of $\sim 150\mu\text{Jy beam}^{-1}$. The SE component appeared to be significantly polarised, at a level of between 5 and 20 per cent. In epochs 1 and 9, the core was also found to be polarised, and in epoch 4 there was marginal evidence for the detection of polarisation in the emerging receding (NW) component.

The polarisation intensity, fractional polarisation, and

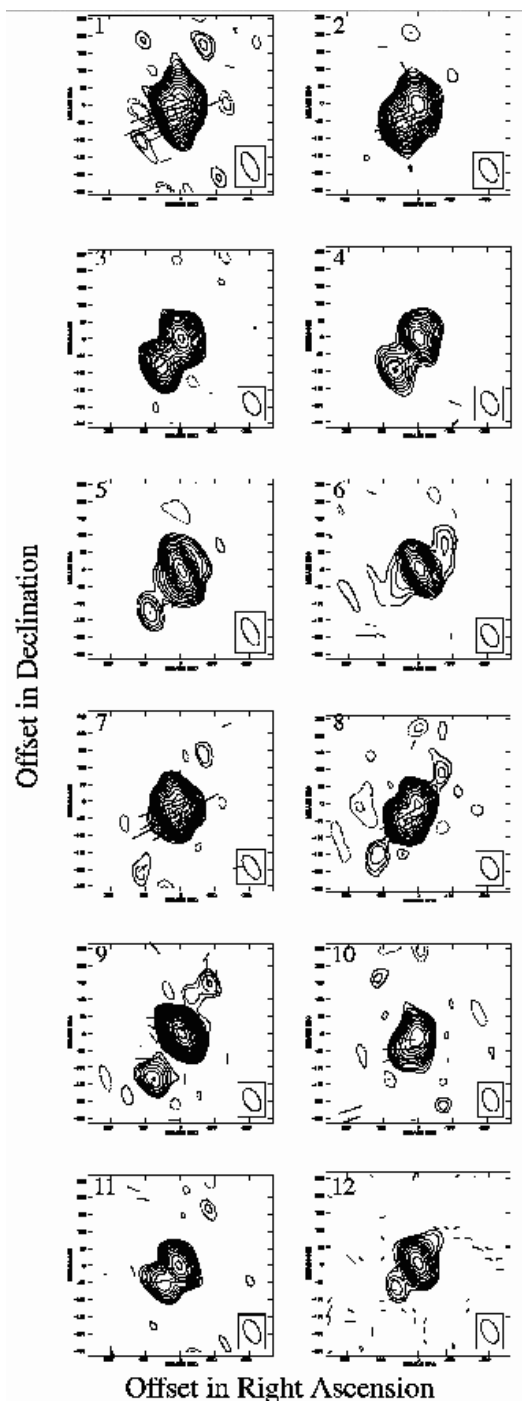


Figure 12. Contour maps with superposed linear polarisation E vectors. Solid and dashed contours are $(\sqrt{2})^n$ and $-(\sqrt{2})^n$ times the $3\text{-}\sigma$ noise level in the image. The lengths of the polarisation vectors are scaled to represent the level of linearly polarised flux density P in the image. A vector of length 100 mas corresponds to $3.33 \text{ mJy beam}^{-1}$. To reduce confusion, only polarisation vectors greater than the $3\text{-}\sigma$ level in the total polarisation image have been plotted, except in the case of epoch 12, where the vectors have been plotted down to the $1\text{-}\sigma$ level. The beam sizes for each image are plotted in the lower right-hand corner. At a distance of 10.9 kpc, 1mas on the image corresponds to a spatial scale of 10.9 au.

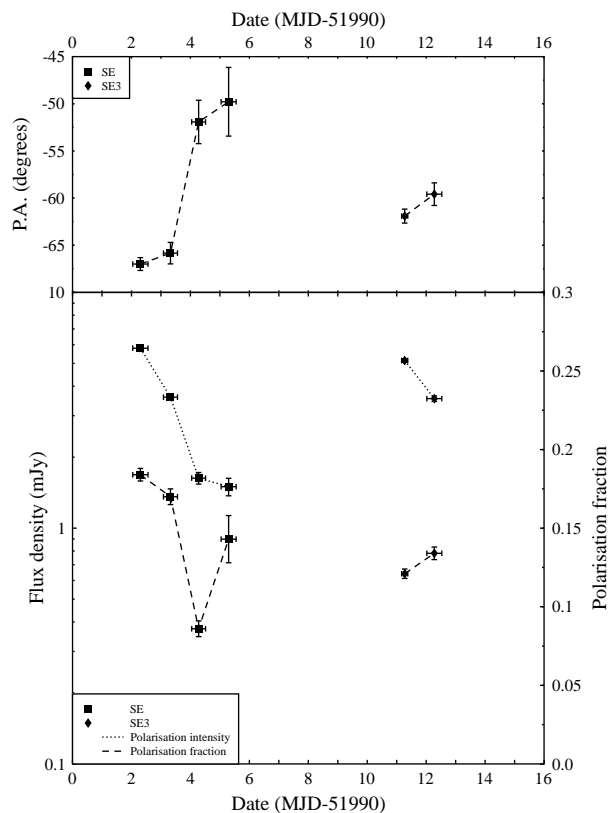


Figure 13. Linear polarisation parameters for the 2001 March outburst. The bottom panel shows the total intensity on the left-hand axis (dotted lines) and the fractional polarisation (dashed lines) on the right-hand axis. The top panel shows the polarisation position angle. The parameters measured for the SE and SE3 components are shown by squares and diamonds respectively.

polarisation position angle for the SE and SE3 components are plotted in Fig. 13. As the component moves outwards, the polarisation position angle rotates, and both the integrated and fractional polarisation decrease. If the change in position angle is due to changing Faraday rotation as the jet component expands and moves outwards, the implied changes in rotation measure for the SE and SE3 components of the March observations are 83.3 rad m^{-2} over the course of 4 days and 11.1 rad m^{-2} over 2 days respectively, whereas the change between epochs 10 and 11 of the July observations is 60.1 rad m^{-2} over 2 days. Without multi-frequency observations, it is not possible to tell whether the observed rotation of the position angle is in fact due to Faraday rotation. But we note that Fender et al. (2002) observed a ‘rotator’ event in 2001 January, when the polarisation position angles at 4.8 and 8.4 GHz rotated together, implying that Faraday rotation was not responsible. A different mechanism is therefore required at times in this source. Such a mechanism could be that the observed jet knot is composed of a series of shocks, which fade at different rates, or even reshock and brighten. As different shocks come to dominate, the observed position angle of the polarisation vector would appear to change if the field lines were oriented differently

in the different shocks. A more exciting possibility however is that we could be seeing genuine rotation of the field lines, either tracing an underlying helical pattern in the field lines at large distances from the core (e.g. Gómez et al., 2001), or possibly even due to rotation of the knots themselves. But with the limited sampling and single frequency monitoring available, we cannot distinguish between these possibilities.

5.2 Circular polarisation

The ATCA observations of Fender et al. (2002) found circular polarisation of -0.56 ± 0.07 mJy (0.32 ± 0.05 per cent) at 4.8 GHz just prior to our observations of epoch 1. Our MERLIN observations put a 3σ upper limit of 0.5 mJy beam $^{-1}$ on the Stokes V flux density during epoch 1 when the source was at its brightest, although the circular polarisation feeds on the MERLIN antennas make Stokes V more susceptible to contamination by Stokes I than is the case for the linearly polarised feeds used on ATCA. The ATCA detections were interpreted as either intrinsic circular polarisation of the synchrotron emission or the conversion of linear to circular polarisation in the synchrotron-emitting plasma. In either case, a low-energy tail to the electron energy distribution is implied.

6 ENERGETICS

Taking the rise time of the flare observed during epoch 6, Δt , as a constraint on the volume of the emitting region, $V = 4\pi(c\Delta t)^3/3$, and assuming that the increase in flux density originates from within this region, then using the formalism of Longair (1994), we can estimate a minimum energy associated with this flare.

$$W_{\min} = 3.0 \times 10^6 \eta^{4/7} \left(\frac{V}{\text{m}^{-3}} \right)^{3/7} \left(\frac{\nu}{\text{Hz}} \right)^{2/7} \left(\frac{L_\nu}{\text{WHz}^{-1}} \right)^{4/7} \text{ J}, \quad (7)$$

where V is the source volume, ν is the frequency at which the luminosity L_ν is measured, and $(\eta - 1)$ is the ratio of energy in protons to that in relativistic electrons. The magnetic field corresponding to this minimum energy criterion (close to but not identical to the equipartition magnetic field), B_{\min} , may be expressed (Longair, 1994) as

$$B_{\min} = 1.8 \left(\frac{\eta L_\nu}{V} \right)^{2/7} \nu^{1/7} \text{ T}. \quad (8)$$

In order to evaluate these quantities, the rise time of the outburst, the frequency and the luminosity must first be calculated in the rest frame of the source. Assuming that the flux density is dominated by the approaching jet, the rise time Δt in the rest frame of the observer is Doppler compressed compared to that in the source frame, τ , as

$$\tau = \delta_{\text{app}} \Delta t = \frac{\Delta t}{\Gamma(1 - \beta \cos \theta)}, \quad (9)$$

The rest frame frequency and flux density may also be found for the approaching component. $\nu = \delta_{\text{app}} \nu'$, where primed quantities denote those in the rest frame of the jet knot, and unprimed quantities those in the observer's frame. Since (S_ν/ν^3) is a Lorentz invariant,

$$S'_\nu = \frac{S_\nu}{\delta_{\text{app}}^{3+\alpha}} = S_\nu (\Gamma[1 - \beta \cos \theta])^{3+\alpha}, \quad (10)$$

where the extra power of α corrects for a source spectrum not being flat. The monochromatic luminosity is expressed as $L_\nu = 4\pi d^2 S'_\nu$. Since this depends on the distance to the source, the inferred minimum energy and minimum energy magnetic field are plotted as a function of source distance in Fig. 14. These are derived under the assumptions that the filling factor of the source is ~ 1 , that the spectral index of the emission is $\alpha = 0.75$ (consistent with the spectral index for the integrated emission derived for this outburst by Fender et al. (2002)), that the radio emission extends over a range in frequency such that $\nu_{\text{max}}^{-(p-2)/2} \ll \nu_{\text{min}}^{-(p-2)/2}$, and that the observing frequency $\nu = \nu_{\text{min}}$, the lowest frequency down to which radio emission is seen. This puts a lower limit on the minimum energy of the outburst. The low-energy tail to the electron energy distribution implied by the circular polarisation observations outlined in § 5.2 would however significantly increase the total energy requirement.

The minimum energy is a more slowly-varying function of source distance than the minimum power, $2E_{\min}/\delta_{\text{app}}\Delta t$ (the factor of two arising from the assumption of symmetric approaching and receding components), since the Doppler factor δ_{app} decreases rapidly as the source distance approaches d_{max} (see Fig. 7).

Knowing the luminosity of the source (in its rest frame) and the minimum energy field, we can estimate the total number of relativistic electrons. For a power-law electron spectrum, $N(E) = \kappa E^{-p} dE$, assuming that the maximum electron Lorentz factor is large, we can express

$$\kappa = (p-1)n_{\text{tot}}(m_e c^2)^{p-1} \gamma_{\min}^{p-1}, \quad (11)$$

where n_{tot} is the electron number density, m_e is the electron mass, and γ_{\min} the minimum electron Lorentz factor. We assume that each electron radiates at frequency

$$\nu = \frac{\gamma^2 e B}{2\pi m_e}, \quad (12)$$

where e is the charge of an electron. Assuming that the minimum Lorentz factor electrons correspond to the observing frequency, we can then use equation (19.17) from Longair (1994) to derive

$$N_{\text{tot}} = \frac{L_\nu}{B} \left[A(\alpha)(p-1)(m_e c^2)^{p-1} \left(\frac{2\pi m_e}{e} \right)^\alpha \right]^{-1}, \quad (13)$$

where N_{tot} is the total number of relativistic electrons. $A(\alpha)$ is given by (Longair, 1994, p. 292), and is equal to 594 for $\alpha = 0.75$.

As explained by Fender et al. (1999), the kinetic energy associated with the bulk motion of the jet knot is given by $(\Gamma - 1)E_{\min}$ for an electron-positron jet, or by

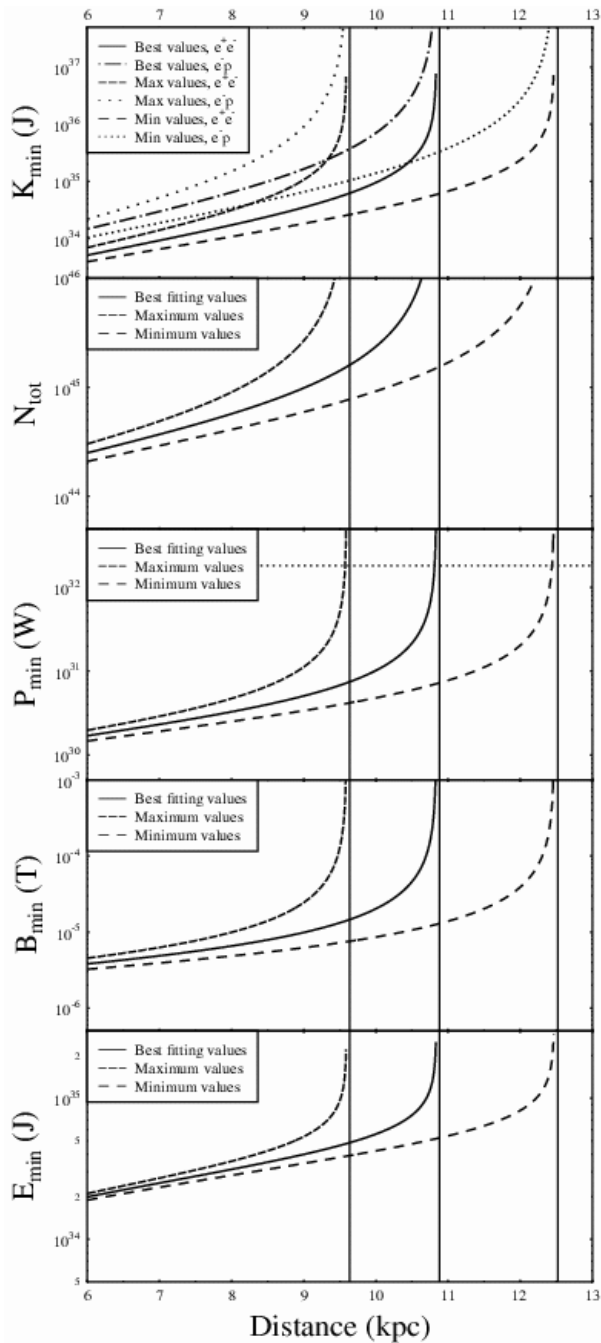


Figure 14. Variation with assumed source distance of minimum energy (E_{\min}), minimum energy magnetic field (B_{\min}), minimum power requirement (P_{\min}), total number of relativistic electrons (N_{tot}), and minimum kinetic energy of jet knot (K_{\min}). Calculations have been done for the best fitting proper motions, the proper motions both low by 1σ (minimum values), and the proper motions both high by 1σ (maximum values). The vertical lines indicate the corresponding values of d_{max} for these cases, 10.9, 12.5, and 9.5 kpc respectively. The dotted line in the minimum power plot shows the Eddington luminosity for a $14M_{\odot}$ black hole.

$(\Gamma - 1)(E_{\min} + N_{\text{tot}}m_p c^2)$ for an electron-proton jet with ‘cold’ protons, where m_p is the proton mass. These two cases are plotted in the top panel of Fig. 14, and, unless d is very close to d_{max} , differ only by a factor 2–3.

The uncertainties in the distance set out in § 3.4 should be borne in mind when considering the values in Fig. 14. The minimum energy, minimum power, and kinetic energy are all lower limits, which would rise if the source was far from equipartition, which is certainly possible given that the jet knot is decaying and expanding, and is thus manifestly not in a steady state. Furthermore, all these estimates would be further increased if, as seems to be the case from the detection of circular polarisation, the electron energy distribution carries on as a power-law down to energies significantly lower than those associated with the observing frequency via Equation 12.

7 PROPER MOTION DISCREPANCY

These observations seem to have confirmed the observed discrepancy between the measured proper motions on milliarcsecond scales, as measured by the VLBA and MERLIN, and those measured on arcsecond scales with the VLA. The proper motions for the SE component of the 1997 October flare found by Dhawan et al. (2000b) over the course of 2.5 h correspond to $22.1 \pm 1.9 \text{ mas d}^{-1}$, consistent with the value of $23.6 \pm 0.5 \text{ mas d}^{-1}$ found with MERLIN for the same event (Fender et al., 1999), and imply no deceleration between 50 and 320 mas. Dhawan et al. (2000b) also imaged discrete ejecta for an event in 1998 May, finding a proper motion of $22.3 \pm 1.7 \text{ mas d}^{-1}$ for the approaching component over the course of 4.5 h. However, Rodríguez & Mirabel (1999) consistently measured proper motions of $\sim 17 \text{ mas d}^{-1}$ with the VLA for four different outbursts in 1994 January–April (including that analysed by Mirabel & Rodríguez, 1994). They saw no evidence for deceleration between 80 and 1420 mas. In this paper, we again measure higher proper motions with MERLIN on scales of 50–300 mas, with no evidence for deceleration.

The discrepancy between the VLA and MERLIN measurements was attributed by Fender et al. (1999) either to intrinsic differences in the jet speeds for the two outbursts, or to resolution effects between the two arrays, whereas Rodríguez & Mirabel (1999) also suggested a possible change in the angle of ejection. Our observations suggest that the jet velocity does not vary dramatically between outbursts, since the proper motions measured for both the 2001 March and July flares were consistent with one another, and with those measured by Fender et al. (1999) and Dhawan et al. (2000b). However, we note that with such a small sample size, this conclusion cannot be regarded as definitive.

As well as the differences in angular resolution between these two seemingly discrepant sets of results, there is also a

difference in the observation dates. All the VLA observations were taken in 1994, while the MERLIN and VLBA data were taken in 1997, 1998 and 2001. This raises the possibility that the discrepancy could be a result of jet precession. If the jet angle had precessed towards us between the 1994 and the 1997 observations, the measured proper motions of the approaching component would be greater owing to relativistic effects. However, those of the receding component would then be correspondingly lower (see fig. 4 of Fender, 2003), in contradiction to the observations. The VLA measured receding proper motions of $7\text{--}9\text{ mas d}^{-1}$, whereas the MERLIN observations give $10\text{--}12\text{ mas d}^{-1}$. Also, we might expect to observe a similar change between the 1997 and 2001 observations as seen between 1994 and 1997, but the former two results are in fact consistent with one another. These arguments would seem to rule out the precession theory, and lend weight to the suggestion of Fender et al. (1999) whereby the lower angular resolution of the VLA resulted in the blending of components and hence lower proper motions. If this is the true explanation however, it begs the question of whether MERLIN itself is resolving the components adequately, and whether with further improved resolution, one would measure still faster proper motions. Certainly none of the MERLIN observations show closely-spaced components that might be blended at the VLA resolution of 200 mas. That all the VLA observations should consist of such superpositions of ejecta, whereas none of the MERLIN observations did seems to be too much of a coincidence. Until this issue is resolved, the derived jet speeds should be considered open to possible future revision upwards, making this source even more energetic than is currently believed. Observations of further outbursts with multiple arrays seem to be required to properly resolve this issue.

A different explanation could be provided by the environment of GRS 1915+105, and the medium into which the jet knots propagated. The source was originally discovered in 1992 August (Castro-Tirado et al., 1992) and has not since returned to full quiescence. BATSE was launched in 1991 April, and Paciesas et al. (1996) state that no flares were detected prior to 1992 May 6. If prior to its discovery in 1992 the source had been in its true quiescent state with a very weak jet, the environment of the source would have been the relatively dense, low-velocity interstellar medium (ISM). An outburst at this time would have quickly run into the ISM, and the interaction between the jet material and the ISM would have determined the advance speed of the external shocks thus generated. We note that the infrared jets in GRS 1915+105 detected by Sams, Eckart & Sunyaev (1996), which have never since been detected, could correspond to the heating of the surrounding ISM by the jet. As the jet/ISM boundary moved further out over time, the jet would have been less energetic at the boundary, and unable to heat the surrounding ISM to detectable levels. Prior to later outbursts, the plateau-state steady jet could have inflated a bubble in the surrounding ISM similar to that seen in Cygnus X-1 (Gallo et al., in prep.), evacuating the region through which the jet propagates. Consequently, in later outbursts we see only the emission from the inter-

nal shocks as the high Lorentz factor jet catches up with the lower-velocity steady jet, since the jet/ISM boundary is considerably more distant from the core of the system. Future VLA observations should therefore measure the same proper motions as those measured by MERLIN and the VLBA. This scenario would imply that the lobes identified by Kaiser et al. (2004) are unlikely to be physically associated with GRS 1915+105, strengthening the case for it to lie at a distance of ~ 11 kpc. We reiterate the need for further VLA observations of the relativistic ejecta during an outburst of GRS 1915+105.

8 JET EJECTION

Vadawale et al. (2003) suggested that the observed flares of GRS 1915+105 with discrete ‘superluminal’ ejecta occurred after a radio-loud hard X-ray state (the C_{RL} state) in which a continuous flat-spectrum jet existed in the radio pre-flare plateau state. They postulated that an X-ray dip into state A corresponded to the ejection of the Comptonising cloud in the core of the system at higher velocity than that of the pre-existing continuous jet, creating an internal shock in the flow which was observed as discrete, fast-moving, radio-emitting ejecta. This model is supported by observational evidence, since Gallo, Fender & Pooley (2003) had previously noted that steady jet outflows for generic black hole X-ray binaries were significantly less relativistic than transient outbursts, whereas in the specific case of GRS 1915+105, lower limits on the speed of the compact jet in the plateau state were found by Dhawan et al. (2000b) and Ribó, Dhawan & Mirabel (2004), who measured speeds of $\beta = 0.1$ and $0.3\text{--}0.4$ respectively.

Fender et al. (1997) made the connection between infrared and radio flares, suggesting that the two had a common origin in synchrotron emission from a jet. Eikenberry et al. (1998) studied the simultaneous infrared and X-ray behaviour of the source, and found a close link between X-ray and infrared flares, including evidence that an X-ray precursor spike was associated with the start of a flare. Finally, Mirabel et al. (1998) made simultaneous X-ray, infrared and radio observations of GRS 1915+105 at two epochs in 1997, and found that the infrared/radio flares were associated with hard X-ray dips, also suggesting that the ejection event occurred at the time of an X-ray spike at the end of the spectral softening.

Fender & Belloni (2004) created a synthesis of the above pictures, together with other work, to suggest that above a certain X-ray hardness, the source produces a steady outflow. As the X-ray spectrum softens, the jet velocity increases monotonically until it crosses some ‘jet-line’, where the soft X-ray flux peaks. At this point, the jet velocity increases rapidly before the jet is shut off, and the faster-moving material causes internal shocks as it collides with the pre-existing flow. These shocks then appear as discrete relativistic ejecta with high bulk Lorentz factors, such as

those we have observed. GRS 1915+105 appears to be continually crossing and recrossing this jet-line, producing the oscillation events such as those reported by Pooley & Fender (1997) as the jet switches on and off. If the source spends sufficient time in the X-ray hard state C, there is enough pre-existing material in the continuous jet for internal shocks to give rise to the discrete, highly relativistic ejecta seen in radio observations. This scenario is discussed in more detail by Fender et al. (2004), who discussed the energetics of the internal shock model, finding that 5–40 per cent of the kinetic energy of the fast jet could be released in the shock, which increases the energy budget of § 6 by up to an order of magnitude. A physical explanation of the above scenario was also proposed, whereby the inner edge of the accretion disc moves closer to the compact object as the accretion rate rises. This is supported by the increase in the frequency of the low-frequency QPOs (figs. 5, 8, and 9 of Vadawale et al., 2003), and the values of the inner disc radius derived from model-fitting to X-ray spectra. The escape velocity from this point therefore rises, increasing the jet Lorentz factor until an internal shock is formed as the jet switches off, the reason for which is not yet entirely clear. Observational evidence for the jet switching off can be seen in Fig. 10, where the core flux density falls to very low levels in epochs 1 and 6 in the immediate aftermath of the ejections of components SE and SE3 of the March outburst sequence.

We see from Fig. 14 that the minimum power involved in launching the jet is of order 1–10 per cent of the Eddington luminosity for a $14M_{\odot}$ black hole, unless the true distance to the source is very close to the calculated d_{\max} , when it is even greater. Gallo et al. (2003) noted that in low/hard state black holes, jet suppression occurs at a constant fraction of a few per cent of the Eddington rate as a source moves into a high/soft state. Thus it appears that the jet could be the dominant power output channel during the last moments before it switches off.

9 CONCLUSIONS

We have observed two flaring sequences from GRS 1015+105 in 2001 March and July. The March sequence showed multiple ejection events, whereas only a single pair of ejecta was observed in July. We measured proper motions of 21.4 ± 2.0 , 24.7 ± 1.0 and 23.8 ± 2.8 mas d^{-1} for the three bright approaching components, and 11.8 ± 2.0 and 11.8 ± 3.5 mas d^{-1} for the two detected receding components, consistent with those found with MERLIN by Fender et al. (1999). The 3σ upper limits on the source distance are 13.9 kpc for the March outburst and 15.1 kpc for the July event.

We propose a possible explanation of the discrepancy between the proper motions measured with the VLA, whereby prior to 1992, the source had been in quiescence, such that the environment surrounding it had been filled in. Subsequently, the jet has inflated a cavity so that internal

shocks propagate through the steady jet unaffected by the external medium.

We have observed linear polarisation arising from the approaching jet component which decreases with increasing angular separation from the core, with a very gradual rotation of polarisation position angle with time. With the current data, we are unable to distinguish between the possibilities of Faraday rotation, brightening and fading of different shocks within the beam, rotation of the knots, or a genuine underlying helical structure in the magnetic field.

We have demonstrated that the energetics of the system, often calculated for an assumed source distance, vary substantially with source distance, which could lie anywhere between 6 and 12.2 kpc according to current estimates. However, the minimum power required for the outburst is 1–10 per cent of the Eddington luminosity for the $14M_{\odot}$ black hole believed to lie at the centre of the system, although this may be more if either the source lies very close to d_{\max} or does not satisfy the minimum energy criterion.

The data provide support for the internal shock model proposed by Kaiser et al. (2000) and refined by Vadawale et al. (2003) and Fender et al. (2004), whereby the jet velocity increases rapidly at the start of an outburst, before shutting off after the Lorentz factor of the ejected material peaks. The increasing velocity causes internal shocks which light up the underlying outflow and appear as discrete ejecta moving outwards from the core with constant velocity. Shocks are only produced once, on crossing the ‘jet line’ from a hard to a soft X-ray state; after the initial ejection, no second set of shocks is seen prior to the source moving back to the X-ray state C with steady nuclear jet emission.

ACKNOWLEDGMENTS

MERLIN is operated as a National Facility by the University of Manchester at Jodrell Bank Observatory on behalf of the Particle Physics and Astronomy Research Council (PPARC). We would like to thank Vivek Dhawan, Michael Rupen, Marc Klein-Wolt, and Tom Maccarone for useful discussions. We also thank Francis Graham-Smith and Bryan Anderson for useful comments following a careful perusal of the manuscript. DGM^c would like to acknowledge receipt of a PPARC studentship during the period of this research.

References

- Belloni T., Méndez M., King A. R., van der Klis M., van Paradijs J., 1997a, *ApJ*, 479, L145
- Belloni T., Méndez M., King A. R., van der Klis M., 1997b, *ApJ*, 488, L109
- Belloni T., Klein-Wolt M., Méndez M., van der Klis M., van Paradijs J., 2000, *A&A*, 355, 271

- Browne I. W. A., Wilkinson P. N., Patnaik A. R., Wrobel J. M., 1998, *MNRAS*, 293, 257
- Castro-Tirado A. J., Brandt S., Lund N., 1992, *IAU Circular*, 5590, 2
- Chapuis C., Corbel S., 2004, *A&A*, 414, 659
- Corbel S., Fender R. P., Tzioumis A. K., Tomsick J. A., Orosz J. A., Miller J. M., Wijnands R., Kaaret P., 2002, *Science*, 298, 196
- Dhawan V., Goss W. M., Rodríguez L. F., 2000a, *ApJ*, 540, 863
- Dhawan V., Mirabel I. F., Rodríguez L. F., 2000b, *ApJ*, 543, 373
- Eikenberry S. S., Matthews K., Morgan E. H., Remillard R. A., Nelson R. W., 1998, *ApJ*, 494, L61
- Fender R. P., 2003, *MNRAS*, 340, 1353
- Fender R. P., Belloni T., 2004, *ARA&A*, 42, 317
- Fender R. P., Pooley G. G., Brocksopp C., Newell S. J., 1997, *MNRAS*, 290, L65
- Fender R. P., Garrington S. T., McKay D. J., Muxlow T. W. B., Pooley G. G., Spencer R. E., Stirling A. M., Waltman E. B., 1999, *MNRAS*, 304, 865
- Fender R. P., Rayner D., McCormick D. G., Muxlow T. W. B., Pooley G. G., Sault R. J., Spencer R. E., 2002, *MNRAS*, 336, 39
- Fender R. P., Gallo E., Jonker P. G., 2003, *MNRAS*, 343, L99
- Fender R. P., Belloni T. M., Gallo E., 2004, *MNRAS*, 355, 1105
- Fender R. P., Maccarone T. J., van Kesteren Z., 2005, preprint (astro-ph/0504205)
- Gómez J., Marscher A. P., Alberdi A., Jorstad S. G., Agudo I., 2001, *ApJ*, 561, L161
- Gallo E., Fender R. P., Pooley G. G., 2003, *MNRAS*, 344, 60
- Greiner J., Cuby J. G., McCaughrean M. J., Castro-Tirado A. J., Mennickent R. E., 2001, *A&A*, 373, L37
- Greiner J., Cuby J. G., McCaughrean M. J., 2001, *Nature*, 414, 522
- Kaiser C. R., Sunyaev R., Spruit H. C., 2000, *A&A*, 356, 975
- Kaiser C. R., Gunn K. F., Brocksopp C., Sokoloski J. L., 2004, *ApJ*, 612, 332
- Klein-Wolt M., Fender R. P., Pooley G. G., Belloni T., Migliari S., Morgan E. H., van der Klis M., 2002, *MNRAS*, 331, 745
- Longair M. S., 1994, *High energy astrophysics. Vol.2: Stars, the galaxy and the interstellar medium*. Cambridge: Cambridge University Press, 2nd ed.
- Miller-Jones J. C. A., Blundell K. M., Duffy P., 2004, *ApJ*, 603, L21
- Mirabel I. F., Rodríguez L. F., 1994, *Nature*, 371, 46
- Mirabel I. F., Dhawan V., Chaty S., Rodríguez L. F., Martí J., Robinson C. R., Swank J., Geballe T., 1998, *A&A*, 330, L9
- Paciesas W. S., Deal K. J., Harmon B. A., Zhang S. N., Wilson C. A., Fishmas G. J., 1996, *A&A*, 120, 205
- Pfenniger D., Revaz Y., 2005, *A&A*, 431, 511
- Pooley G. G., Fender R. P., 1997, *MNRAS*, 292, 925
- Ribó M., Dhawan V., Mirabel I. F., 2004, in Bachiller R., Colomer F., Desmurs J. F., de Vicente P., eds., *Proceedings of the 7th Symposium of the European VLBI Network on New Developments in VLBI Science and Technology*. Observatorio Astronomico Nacional of Spain, p.111
- Roberts D. H., Lehar J., & Dreher J. W., 1987, *AJ*, 93, 968
- Rodríguez L. F., Mirabel I. F., 1998, *A&A*, 340, L47
- Rodríguez L. F., Mirabel I. F., 1999, *ApJ*, 511, 398
- Sams B. J., Eckart A., Sunyaev R., 1996, *Nature*, 382, 47
- Stirling A. M., Spencer R. E., de la Force C. J., Garrett M. A., Fender R. P., Ogle R. N., 2001, *MNRAS*, 327, 1273
- Vadawale S. V., Rao A. R., Naik S., Yadav J. S., Ishwara-Chandra C. H., Pramesh Rao A., Pooley G. G., 2003, *ApJ*, 597, 1023
- Zdziarski A. A., Gierliński M., Rao A.R., Vadawale S. V., Mikołajewska J., 2005, preprint (astro-ph/0504018)